Atmos. Chem. Phys. Discuss., 11, 1053–1104, 2011
www.atmos-chem-phys-discuss.net/11/1053/2011/
doi:10.5194/acpd-11-1053-2011


Atmospheric Chemistry and Physics Discussions



# A spectral method for retrieving cloud optical thickness and effective radius from surface-based transmittance measurements

**P. J. McBride**[1,2], **K. S. Schmidt**[1], **P. Pilewskie**[1,2], **A. S. Kittelman**[2], **and D. E. Wolfe**[3]

[1]Laboratory for Atmospheric and Space Physics, University of Colorado, Campus Box 392, Boulder, CO 80309-0392, USA
[2]Department of Atmospheric and Oceanic Sciences, University of Colorado, Campus Box 311, Boulder, CO 80309-0311, USA
[3]NOAA Earth Systems Research Laboratory, Physical Science Division, Weather and Climate Physics Branch, 325 Broadway, Boulder, CO 80305, USA

Received: 6 October 2010 – Accepted: 10 December 2010 – Published: 17 January 2011

Correspondence to: P. J. McBride (patrick.mcbride@colorado.edu)

Published by Copernicus Publications on behalf of the European Geosciences Union.







## Abstract

We introduce a new multispectral method for the retrieval of optical thickness and effective radius from cloud transmittance, which is less sensitive to effective radius than cloud reflectance. Based on data from the moderate spectral resolution observations of the Solar Spectral Flux Radiometer (SSFR) and Shortwave Spectroradiometer (SWS), we use the spectral shape of transmitted radiance as a means of retrieving effective radius from cloud transmittance. The observations were taken during the International Chemistry Experiment in the Arctic Lower Troposphere and at the Southern Great Plains (SGP) site of the Atmospheric Radiation Measurement (ARM) Climate Research Facility. The spectral shape was quantified by fitting a slope to the normalized transmittance between 1565 nm and 1634 nm. The retrieval was performed by comparing the observed slope at 1565 nm and the transmittance at 515 nm with a pre-calculated library (lookup table). An estimate of the retrieval uncertainty was provided by propagating the uncertainty of the observations through the best-fit algorithm. We compare the new retrieval with an algorithm that uses transmittance at two wavelengths, a method often used with cloud reflectance. The liquid water path (LWP) is derived from the retrieved optical thickness and effective radius, assuming a cloud with effective radius varying linearly with altitude above cloud base, and compared to the retrieved liquid water path from a microwave radiometer. Retrievals from two MODIS overpasses of the SGP were also compared. The data taken from the SGP was under thicker cloud than the case used from ICEALOT, with average optical thickness of 44 and 22, respectively. For the time period with the thicker clouds, the dual-wavelength method and the slope method retrieved nearly indistinguishable results. The dual-wavelength method, however, resulted in slightly higher average relative effective radius uncertainty of 12.9 µm±12.8%, as compared to 12.8 µm±8.9% from the slope method. The thinner cloud case resulted in a significant difference between the dual-wavelength and slope algorithms with average retrieved effective radius and uncertainties of 12.5 µm±8.4% and 17.0 µm±21.0% for the slope and dual-wavelength methods, respectively. The





ACPD
11, 1053–1104, 2011



retrieved optical thickness values for this case were nearly identical. The average derived LWP was within 12.5% and 20% of the MWR LWP for the ARM and ICEALOT data. For a homogeneous cloud case, the MODIS retrievals (optical depth, effective radius, and LWP) were within the uncertainty of the SWS retrievals. Inhomogeneous clouds resulted in lesser agreement between the MODIS and SWS retrievals.

## 1 Introduction

Clouds are an important regulator to the flow of radiant energy in the atmosphere through the processes of scattering and absorption of shortwave and longwave radiation. They cool the Earth by reflecting incoming solar radiation to space and warm the Earth's surface and lower atmosphere by their emission of infrared radiation. Despite decades of cloud observations, there is still not a complete understanding of their role in the climate system. For one, clouds have not been studied from the surface in any global, systematic way. Aerosol optical thickness is observed on a global scale at the surface through the Aerosol Robotic Network (AERONET) program (Holben, 1998). Cloud properties are cataloged and studied through the satellite observations included in the International Satellite Cloud Climatology Project (Schiffer and Rossow, 1983). These are both long term and global datasets that provide essential trends in cloud and aerosol properties. A similar catalog of data would be useful with cloud properties observed from the surface. Such observations also have a large potential for studying the effect of aerosols on clouds. The Intergovernmental Panel on Climate Change (IPCC) lists the effects of aerosol on clouds as the largest uncertainty in the forecasting of future climate change (Forster et al., 2007).





ACPD
11, 1053–1104, 2011



Cloud optical thickness ($\tau$=column integrated extinction) and effective radius ($r_{\text{eff}}$) (Hansen and Hovenier, 1974):

$$r_{\text{eff}} = \frac{\int_0^\infty Q_{\text{ext}}(r) r^3 n(r) dr}{\int_0^\infty Q_{\text{ext}}(r) r^2 n(r) dr} \quad (1)$$

where $Q_{\text{ext}}$ is the extinction efficiency and $n(r)$ is the cloud particle size distribution, can be derived from cloud reflectance because reflectance steadily increases with optical thickness up to an asymptotic limit, determined by the spectrally dependent bulk water absorption. In the weak absorption/geometric optics limit of this spectral domain, effective radius is proportional to the absorption coefficient (Twomey and Bohren, 1980). Transmitted radiance is more difficult to exploit for cloud retrievals, for two reasons. Firstly, downward radiance first increases with optical thickness (due to enhanced diffuse radiation with increasing number concentration of scattering particles) and then decreases due to attenuation. Therefore, the inversion of transmittance is double-valued with respect to optical thickness, with a thin-cloud and a thick-cloud solution. Secondly, the asymptotic value that is reached for high optical thickness is always the same (zero), regardless of wavelength and droplet size, which makes the transmitted signal less sensitive to effective radius.

Cloud retrieval methods have been developed using reflected solar radiation with data collected from satellite and airborne sensors (for example, Hansen and Pollack, 1970; Twomey and Cocks, 1989; Nakajima and King, 1990, among many others). Airborne and satellite based retrievals are able to cover large areas and provide an important global perspective of clouds. However, Platnick (2000) modeled photon transport through clouds and calculated the weighting functions for transmittance and reflectance. The weighting function quantifies the contribution of a cloud layer to the observed transmittance or reflectance. The results showed that the upper layers of the cloud are weighted more heavily, meaning that these layers are sampled preferentially





ACPD
11, 1053–1104, 2011



over lower layers of the cloud. This can lead to erroneous retrieval results, depending on the vertical distribution of cloud particle size. Cloud transmittance is more evenly weighted throughout the cloud layers. This demonstrates that cloud transmittance provides a perspective that is unique from cloud reflectance and important in our understanding of clouds.

Cloud retrieval methods using transmitted radiation have been developed more recently than cloud reflectance methods. Leontyeva and Stamnes (1994) used transmitted broadband irradiance which has a one-to-one relationship with optical thickness. Barker and Marshak (2001) used a combination of irradiance and radiance at two wavelengths to retrieve cloud optical thickness under broken cloud conditions and over a vegetated surface. Marshak et al. (2004) continued this work by demonstrating a technique to retrieve optical thickness and effective cloud fraction from transmitted radiance at 673 nm and 870 nm over vegetated surface. The ratio of the difference to the sum of the two radiances is used and they show that this technique overcomes the lack of a one-to-one radiance to optical thickness relationship. This same approach was applied to AERONET data by Chiu et al. (2010) replacing the radiance at 673 nm with radiance at 440 nm. Efforts have been made to retrieve both optical thickness and cloud particle effective radius. Rawlins and Foot (1990) used the ratio of cloud transmittance at 1550 nm to 1040 nm and the transmittance at 1040 nm to retrieve optical thickness and effective radius. They found, however, that the effective radius retrievals were not significant given the high uncertainty in the retrievals. Kikuchi et al. (2006) used absolute transmittance measured at three wavelengths, 1020 nm, 1600 nm, and 2200 nm to retrieve optical thickness and effective radius.

The objective of this paper is to demonstrate the potential of spectral radiance to retrieve cloud optical thickness and cloud particle effective radius of homogeneous clouds using observations from a single instrument. The technique introduced in this paper achieves this goal by capitalizing on the measurement of a continuous spectrum. It is similar to methods previously employed to determine cloud thermodynamic phase (Pilewskie and Twomey, 1987; Ehrlich et al., 2008) in that, in addition to the relative





ACPD
11, 1053–1104, 2011



magnitude of spectral signal, the spectral shape of reflected radiance is exploited. In this study we derive cloud optical thickness and droplet effective radius using the spectral slope of the transmitted radiance between 1565 and 1634 nm, normalized to its value at 1565 nm. This technique avoids the ambiguity of the transmitted radiance with respect to optical thickness and allows for the retrieval of effective radius with relatively low uncertainty compared to other methods. By normalizing the transmittance, the observations are insensitive to the absolute radiometric calibration of the instrument, assuming that systematic errors are spectrally neutral.

The uncertainties in the retrieved parameters were estimated for the new technique and for a traditional dual-wavelength approach. We show that improved spectral resolution decreases the retrieval error, increases sensitivity to the effective radius, and show the dependence of retrieval accuracy on optical thickness and effective radius. We compare SSFR/SWS-retrieved optical thickness and effective radius with satellite observations for two applications: (1) retrievals from SSFR onboard a research vessel and (2) retrievals from SWS at the Southern Great Plains (SGP) site of the Atmospheric Radiation Measurement (ARM) Climate Research Facility. From the retrieved optical thickness and effective radius, the liquid water path can be approximated as:

$$\mathrm{LWP} = \frac{2}{3}\tau r_{\mathrm{eff}} \tag{2}$$

assuming the cloud droplets are in the geometric optics limit (where $r_{\mathrm{eff}}$ is much larger than the wavelength) and that the cloud is homogeneous, including the vertical distribution of effective radius and liquid water content. Another formulation of the LWP was derived by Wood and Hartmann (2006) for clouds where $r_{\mathrm{eff}}$ varies linearly with altitude above cloud base (referred to hereafter as a WH06 cloud):

$$\mathrm{LWP}_{\mathrm{WH06}} = \frac{5}{9}\tau r_{\mathrm{eff}} \tag{3}$$

In this paper, the LWP is derived using both formulations and compared to the retrievals from a microwave radiometer; the optical thickness retrieval is also compared with





ACPD
11, 1053–1104, 2011



reflectance-based MODIS retrievals. In Sect. 2, we describe the instruments used, the radiative transfer model, the field experiments and the associated data. In Sect. 3, we describe the retrieval techniques and the derivation of retrieval uncertainty. Results are shown in Sect. 4 and conclusions in Sect. 5.

## 2 Instrumentation, experiments, and model

The retrieval method employed in this study used solar spectral radiance data collected with the Solar Spectral Flux Radiometer (SSFR, Sect. 2.3) (Pilewskie et al., 2003) onboard the Woods Hole Oceanographic Institution research vessel Knorr, and data from the ARM Shortwave Spectrometer (SWS, Sect. 2.4) at the DOE ARM Southern Great Plains (SGP) (Stokes and Schwartz, 1994) site (Sect. 2.2). The SSFR was originally designed for airborne zenith and nadir solar spectral hemispherical irradiance measurements. For ground-based and ship-borne observations, one of the irradiance light collectors was replaced with a zenith-viewing radiance fore-optic. The ground-based version of SSFR measured downward radiance and irradiance simultaneously. This is the configuration that was used onboard the Knorr during the International Chemistry Experiment in the Arctic Lower Troposphere (ICEALOT, Sect. 2.1). SWS, in contrast, measured downward radiance only. To validate SSFR and SWS retrievals, simultaneous microwave radiometer (MWR, Sect. 2.5) observations and satellite retrievals from the Moderate Resolution Imaging Spectroradiometer (MODIS, Sect. 2.6) were used.

### 2.1 International Chemistry Experiment in the Arctic Lower Troposphere (ICEALOT)

ICEALOT was conducted by the National Oceanic and Atmospheric Administration within the International Polar Year 2008. The cruise began at the Woods Hole Oceanographic Institution in Woods Hole, MA and headed south into Long Island Sound. From there it headed north, into the ice-free regions of the Northern Atlantic and Arctic





ACPD
11, 1053–1104, 2011



Oceans during March and April, 2008. The focus of ICEALOT was on the transport of springtime pollutants into the Arctic, including the impact of aerosol particles on cloud microphysical properties. The ship payload consisted mainly of gas-phase chemistry and in-situ aerosol instrumentation, but also included cloud remote sensing instruments, a microwave radiometer, a millimeter cloud radar, and a Vaisala ceilometer. The radiance data of the SSFR was used for cloud remote sensing while the irradiance data constrained the radiative energy balance under cloud- and aerosol-laden conditions.

### 2.2 Southern Great Plains site of the ARM climate research facility

One of the missions of the ARM program is the development and maintenance of highly instrumented field stations to constrain the radiative forcing of clouds and aerosols by measurements at the surface. The SGP, located in Lamont, OK, is one of these facilities. The SWS (described in Sect. 2.4) was added to the instrument suite in 2006 to enhance cloud remote sensing capabilities. Diffuse and direct irradiance at selected wavelengths are routinely measured by the Multi-filter Rotating Shadowband Radiometer (MFRSR) (Harrison et al., 1994). Among many other instruments, the site also hosts a sun photometer as part of AERONET, a Vaisala ceilometer, a Total Sky Imager and a microwave radiometer, all relevant to the present study.

### 2.3 Solar Spectral Flux Radiometer (SSFR)

The SSFR is a spectrometer system with moderate spectral resolution (8–12 nm) and sampling frequency (1 Hz). It covers a wavelength range from 350 nm to 1700 nm. It has a collimator for radiance measurements and a hemispheric cosine response light collector for irradiance. Each SSFR system consists of two spectrometers that are connected by an optical fiber to the light collectors mounted on the top (zenith viewing) and bottom (nadir viewing) of an aircraft, or on a zenith-viewing stabilizing platform on one of the towers of a ship. The full spectral range is achieved using a pair of monolithic miniature Zeiss spectrometer modules: a flat-field grating with a linear silicon diode





ACPD
11, 1053–1104, 2011



array detector for the spectral range from 350 nm to 1000 nm, and an Indium-Gallium-Arsenide (InGaAs) linear diode array for the range from 900 nm to 1700 nm (ship version, "PGS1.7"). The silicon module is temperature-stabilized at 27.0 °C±0.3 °C to keep dark currents stable. Its spectral resolution as prescribed by the full-width-half-maximum (FWHM) is 8 nm, with 3 nm sampling resolution. Each observation point has a quasi-Gaussian spectral bandpass or slit function that is 8 nm FWHM. The InGaAs diode array is thermoelectrically cooled to 10.0 °C±0.1 °C (PGS1.7). The temperature of the pre-amplifier and control electronics is stabilized to reduce dark current drift. The FWHM is 12 nm, with 5.5 nm sampling (PGS1.7).

The irradiance light collectors are designed to provide a near-ideal cosine-weighting of the incoming hemispherical radiance. This is realized by a circular aperture in a miniature integrating sphere, covered by a quartz dome for weather protection. Deviations from ideal cosine response are measured in the laboratory and are corrected in post-processing. While the irradiance light collector has a $2\pi$ steradian field of view (FOV), the collimator limits the FOV to 3° for radiance measurements. The angular response of the collimator is also measured in the laboratory before and after each deployment. The rejection of radiation coming from outside the FOV was determined to be better than $10^{-3}$.

Dark current measurements are made every 5–30 min by activating a light shutter in front of the spectrometers for 10–60 s. The rate of the dark current measurements must be higher than the characteristic frequency of the temperature variation within the instrument. For example, if the temperature stabilization cycles with $T$ =30 min, the dark current acquisition frequency needs to be set to at least 4 per 30 min. This is important in the long-wavelength end of the spectral range because they are the most affected by temperature-induced changes in the dark currents due to the strong wavelength dependence in Planck emission. The dark spectra are subtracted from the measured spectra. Between individual dark current measurements, the dark spectra are linearly interpolated.





ACPD
11, 1053–1104, 2011



The radiance calibration is performed at the NASA Ames Research Center with a NIST traceable 30 inch diameter integrating sphere, the same sphere used to calibrate the MODIS airborne simulator (King et al., 1996). The sphere contains 12 NIST traceable quartz-halogen lamps, three of which were illuminated for the SSFR radiance calibration. The radiance output from the sphere is known to within 1–2%. These calibrations were performed before and after deployment. For normal SSFR airborne operations, field calibrations were conducted regularly to track the stability of the instrument. However, for ship-board deployments there was no field-portable sphere that travels with the instrument.

Irradiance calibrations were performed before and after each experiment in the laboratory with a NIST-traceable blackbody (tungsten-halogen 1000 W FEL lamp). The nominal accuracy was 1–3% due primarily to the uncertainty of the calibration light source. The calibration-to-calibration variability was well below 3%. Typically, a calibration stability of 1% or 2% was achieved over the course of a multi-week field mission. Noise-induced errors are only relevant near the edges of the individual spectrometers, below 370 nm and above 950 nm for the Silicon spectrometers and below 950 and above 1650 nm/2100 nm for the InGaAs spectrometers. Typically, precision of 0.1% was achieved, well below the radiometric uncertainty.

### 2.4 Shortwave Spectroradiometer (SWS)

The design of the SWS derives its heritage from the SSFR and is equipped with the InGaAs PGS2.2 spectrometer, extending its spectral range to 2200 nm. The SWS has only one zenith pointing light collector with a field of view of 1.4°, which is about half that of the radiance light collector on the SSFR. The light rejection of the collimator, which limits the field-of-view, was determined to be $10^{-3}$. For measurements under cloud-free or broken cloud conditions, there may be stray light contamination in the near-infrared where molecular scattering is weak, but for the present study under uniform cloud cover (see the discussion on filtering in Sect. 3.5) this level of rejection was adequate. A new SSFR radiance fore-optic with an improved rejection of $10^{-5}$





ACPD
11, 1053–1104, 2011



was deployed in the CALNEX campaign in May, 2010. The same 30 inch sphere was used to calibrate the SWS at NASA Ames once per year. In addition to the 30 inch sphere, the SWS was also calibrated against a portable 12 inch sphere (Labsphere, Inc.). Measuring the response to the two spheres at the same time and under the same conditions allowed the calibration to be transferred from the NIST traceable sphere to the 12 inch sphere. This 12 inch sphere was used in the field for weekly calibrations, conducted by the staff at the SGP, to track changes in the performance of the instrument. The uncertainty of the radiance measurements of the SWS spectrometers is the same as in the SSFR, 1–3%. The SWS had the same temperature stabilization as the SSFR for its spectrometers and was kept in a climate controlled trailer at the SGP. The InGaAs spectrometers had a small drift associated with thermal emission in their spectral response at the longest wavelengths (~2 μm). To correct for this drift, dark current readings were taken every 5 min for 15 s. The dark currents were acquired when a shutter, controlled by the system software of the SWS, closed for a defined frequency and duration. The frequency and duration were stored in a control file and could be easily changed by a remote user. A linear interpolation scheme was used between dark current measurements to account for the temperature changes.

### 2.5 Microwave radiometer

The ARM microwave radiometer measured microwave emissions from the atmosphere at two frequencies to retrieve column integrated liquid water and water vapor. The observations were made at 23.8 GHz and 31.4 GHz, the former being more sensitive to water vapor and the latter more sensitive to liquid water. The instrument measured the emission for 1 s, every 16 s, with a field of view of 5.9° for the 23.8 GHz channel and 4.5° for the 31.4 GHz channel. The uncertainty of the liquid water path observations were approximately ±20 g/m$^2$. The ARM retrieval algorithm was described in Westwater (1993) and Liljegren and Lesht (1996). The NOAA microwave radiometer is very similar to the ARM instruments. It measures at the same frequencies but the fields-of-view are slightly different, 5.7° and 4.4° for the 23.8 and 31.4 GHz channels, respectively. The





ACPD
11, 1053–1104, 2011



underlying premise of the NOAA two-frequency retrieval was the same and the details can be found in Westwater et al. (2001).

### 2.6 Moderate Resolution Imaging Spectroradiometer (MODIS)

MODIS on Aqua and Terra measures radiation in visible, near infrared, and thermal infrared to derive cloud properties at 1 km resolution. The 1 km cloud properties can be found in the MOD06 and MYD06 MODIS products. The cloud retrieval algorithm was presented in Nakajima and King (1990) and Platnick et al. (2003). The algorithm used cloud reflectance at two wavelengths, one in a non-absorbing region for water, and the other in an absorbing region. For retrievals over land, the wavelengths were chosen at 650 nm from the non-absorbing region and at 2100 nm from the absorbing region (Platnick et al., 2003). The former provides mostly optical thickness information and the latter provides mostly cloud particle effective radius information.

### 2.7 Radiative transfer model

One method of retrieving cloud parameters (see for example, Nakajima and King, 1990; Twomey and Cocks, 1989) requires calculating radiances or irradiances for a range of cloud optical thickness, effective radius, solar zenith angles, viewing angles, and wavelengths, to infer the cloud properties from observed radiances or irradiances by finding the best match between calculated and observed values. To avoid the effects of molecular absorption, the radiances and irradiances are chosen outside of the regions of strong molecular absorption.

The plane-parallel radiative transfer model used in this study was adapted from the work of Coddington et al. (2008) and Bergstrom et al. (2003). Downward radiance at the surface was calculated for optical thickness ranging from 0.1 to 0.9 at an interval of 0.1 and from 1 to 100 at an interval of 1. The effective radius was varied from 1 µm to 30 µm at an interval of 1 µm. The radiance data were interpolated to a resolution of 0.1 in optical thickness and 0.1 µm in effective radius. The cosine of the solar zenith angle





ACPD
11, 1053–1104, 2011



was varied from 0.05 to 0.95 at steps of 0.05. Inputs to the model were the spectral surface albedo, elevations at each layer, any cloud parameters, temperature, pressure, and gaseous concentrations. Both the SGP and ICEALOT retrievals were performed using a standard mid-latitude summer atmospheres for the gaseous concentrations and temperature and pressure profiles from radiosonde data obtained from each site.

The spectral surface albedo was another input to the radiative transfer model. The surface at the SGP site consists of a few varieties of vegetation that vary with the growing season. The analysis here focused on spring and summer when the surface was predominately green vegetation. There have been no surface albedo measurements made with the spectral range and resolution of the SWS since its deployment at the ARM site. MODIS (Sect. 2.6) provides 500 m spatial resolution surface albedo across the range of the SWS, but at only a few discrete channels (MODIS products MCD/MOD43A4). To parameterize surface albedo for the forward model, the discrete bands of the MODIS retrieved surface albedo were extended to approximate the spectral shape of a vegetated surface. For the spectral region between 1565 nm and 1634 nm, a green grass albedo from the US Geological Survey (USGS) (Clark et al., 2007) was used. The resultant surface albedo is shown in Fig. 1 along with the USGS green grass albedo. The ICEALOT data was collected over ocean, which has an albedo near 0.03–0.04 and does not vary appreciably over the spectral range of the SSFR/SWS. The spectral ocean albedo (Fig. 1) was retrieved during the International Consortium for Atmospheric Research on Transport and Transformation (Coddington et al., 2008).

Assumptions made in the configuration of the radiative transfer model limit the applicability of the retrieval algorithm. The plane-parallel assumption in the model is best for homogeneous cloud fields. Cases that exhibit strong 3-D structure can lead to erroneous results and misinterpretation. Another assumption is that the clouds consist of liquid water particles. The presence of ice in a cloud may also result in an erroneous retrieval due to the differences in the absorption and scattering properties between liquid water droplets and ice crystals. Efforts to restrict the analysis to homogeneous





ACPD
11, 1053–1104, 2011



clouds composed of liquid will be explained in Sect. 3.

## 3 Retrieval techniques

To develop the retrieval algorithm, calculations with the radiative transfer model were used to examine the relationship of optical thickness and effective radius with reflected ($I_{refl}$) and transmitted radiance ($I_{trans}$). The differences in reflected and transmitted radiance are discussed in Sect. 3.1. In Sect. 3.2, a dual-wavelength retrieval, often used with cloud reflectance (see for example Nakajima and King, 1990), was applied to modeled cloud reflectance and transmittance in order to quantify the sensitivity of cloud optical thickness and effective radius on reflectance and transmittance. Cloud reflectance and transmittance were defined as follows:

$$T = \pi I_{trans}/\mu_0 F_0 \quad R = \pi I_{refl}/\mu_0 F_0 \tag{4}$$

where $I_{trans}$ and $I_{refl}$ are transmitted and reflected radiance, $\mu_0$ is the cosine of the solar zenith angle, and $F_0$ is the irradiance at the top of the atmosphere. To help explain the spectral dependence of cloud droplet absorption and scattering, Mie calculations were employed to calculate: (1) single scattering albedo ($\varpi_0$), the probability that a photon will be scattered in a single interaction with a particle, (2) the asymmetry parameter ($g$), the first moment of the scattering phase function, and (3) cloud optical thickness. To focus on droplet absorption, the coalbedo ($1-\varpi_0$), the probability that a photon will be absorbed in a single interaction with a particle, was calculated and plotted along with the asymmetry parameter in Sect. 3.3. Cloud transmittance was calculated as function of optical thickness and effective radius and is shown in Sect. 3.4. The resulting retrieval algorithm is presented in Sect. 3.5.





ACPD
11, 1053–1104, 2011



### 3.1 Transmitted and reflected radiance as functions of effective radius and optical thickness

Modeled cloud reflectance and transmittance for two effective radius (5 µm and 25 µm) and two wavelengths (515 nm and 1628 nm) are shown in Fig. 2. The behavior of radiance with increasing optical thickness is illustrated in Fig. 2: radiance increases with optical thickness from 0 to approximately 4 or 5, beyond which it decreases with increasing optical thickness. In contrast, the reflected radiance increases monotonically with optical thickness, providing a unique relationship between optical thickness and radiance.

Another difference between reflectance and transmittance is in the sensitivity to effective radius. With increasing optical thickness, reflected radiance approaches an asymptotic value determined by the single scattering albedo or alternatively, particle size. At 515 nm, where water is non-absorbing, the difference in reflectance, for a cloud with effective radius of 5 µm versus 25 µm, is no more than 10% across the optical thickness range between 0.1 and 100.

The transmitted radiance reached at 515 nm is dependent on the optical thickness. At 1628 nm absorption decreases the reflectance from its conservative scattering limit by an amount that depends on droplet size. This forms the basis for cloud retrievals from multi-spectral measurements of cloud reflectance. At wavelengths where liquid water absorbs, the reflected radiance depends primarily on effective radius. At the non-absorbing wavelengths, reflected radiance depends primarily on cloud optical thickness.

The relationship between spectral radiance and cloud optical thickness and effective radius is not as straightforward with cloud transmittance. As optical thickness increases, the transmitted radiance approaches zero (complete attenuation) at all wavelengths, albeit at a rate that varies with the magnitude of droplet absorption. This lack of a unique asymptote in transmittance contributes to the reduction in sensitivity to effective radius compared to the reflectance counterpart, especially for large values of





ACPD
11, 1053–1104, 2011



optical thickness (beyond 40). In addition, changes in effective radius result in smaller net changes in transmittance than in reflectance. For example, if the effective radius is increased, all else being equal, cloud reflectance will be decreased both through increased absorption and increased forward scattering. Cloud transmittance, on the other hand, increases due to increased forward scattering but decreases due to increased absorption. These opposing trends lessen the sensitivity of transmittance to effective radius.

Figure 3a shows the reflectance at a wavelength where liquid water is weakly absorbing (1628 nm) and at a wavelength where liquid water is non-absorbing (515 nm), for a range of effective radius and optical thickness. The reflectance at 515 nm and 1628 nm monotonically increase with optical thickness. The radiance at 515 nm approaches an asymptotic value of 1 for large optical thickness while the radiance at 1628 nm approaches a value less than 1 that is determined by the effective radius. The combination of the two reflectance measurements provides a dataset that is nearly orthogonal in cloud optical thickness and effective radius for optical thickness greater than about 5.

Figure 3b is the same as Fig. 3a except it shows transmittance. As in Fig. 2, transmittance increases with optical thickness between 0 and approximately 4, then decreases beyond that maximum. Lines of constant effective radius are nearly indistinguishable for clouds with optical thickness below 10 and droplet radius larger than 3 µm, consistent with the behavior of the transmitted radiance in Fig. 2. They separate more clearly for optical thickness between 10 and 15. The transmittance at each wavelength approaches complete attenuation for the largest optical thickness. The lines of constant optical thickness are much more clearly delineated than the effective radius lines. This plot implies that there is sensitivity to the optical thickness, virtually no sensitivity to effective radius for optical thickness less than 10, with some sensitivity to effective radius for optical thickness between 20 and 40.





ACPD
11, 1053–1104, 2011



### 3.2 Modeled dual-wavelength retrieval with reflectance and transmittance

To quantify the sensitivity of reflectance and transmittance to cloud optical thickness and effective radius, cloud property retrievals were simulated using modeled cloud reflectance and transmittance for an effective radius of 10 µm and optical thickness of 10, 20, and 40. These cloud parameters were subsequently retrieved using the look up table method described above. The 3% radiometric uncertainty was propagated through the retrieval algorithm to estimate the uncertainty in the retrieved optical thickness and effective radius. These retrieval uncertainties can be used to quantify the sensitivity to the cloud optical properties.

The dual-wavelength retrieval was performed using a least squares fit to determine the best fit between measured and calculated reflectance and transmittance:

$$\chi = \sqrt{\frac{1}{2}\left(\left(\frac{T_{\text{obs},515} - T_{\text{mod},515}}{T_{\text{mod},515}}\right)^2 + \left(\frac{T_{\text{obs},1628} - T_{\text{mod},1628}}{T_{\text{mod},1628}}\right)^2\right)} \tag{5}$$

$T$ is the transmittance and the subscripts mod and obs refer to modeled and observed, respectively. The uncertainty in this equation, resulting from the radiometric uncertainty only, can be propagated to $\chi$ with

$$\delta\chi = \sum_{n=0}^{1}\left(\frac{\partial\chi}{\partial T_n}\delta T_n\right)^2 \tag{6}$$

from Taylor (1996), where $\delta\chi$ is the uncertainty in $\chi$ and $\delta T$ is the 3% radiometric uncertainty, assuming that the uncertainties are Gaussian and independent.

The retrieved optical thickness and effective radius were found by minimizing $\chi-\delta\chi$ and $\chi+\delta\chi$ and using the range of optical thickness ($\tau_{\chi-\delta\chi}$, $\tau_{\chi+\delta\chi}$) and effective radius ($r_{\chi-\delta\chi}$, $r_{\chi+\delta\chi}$). The mean for each effective radius and optical thickness range was taken as the retrieved value:

$$r_{\text{eff}} = \frac{r_{(\chi+\delta\chi)} + r_{(\chi-\delta\chi)}}{2} \tag{7}$$





ACPD
11, 1053–1104, 2011



The uncertainty was defined as half the difference of the range:

$$\delta r_{\text{eff}} = \frac{\left| r_{(\chi+\delta\chi)} - r_{(\chi-\delta\chi)} \right|}{2} \tag{8}$$

Since $\chi$ must be 0 or greater by definition, cases with negative values of $\chi - \delta\chi$ were considered indistinguishable solutions and all these optical thickness and effective radius pairs were included in the retrieved range. For these cases, $r_{\chi+\delta\chi}$ and $r_{\chi-\delta\chi}$ were replaced with the maximum and minimum effective radius in this range. The same is done for optical thickness.

The results of these simulated retrievals are summarized in Table 1. For reflectance above a cloud with an optical thickness of 10, the relative effective radius uncertainty was 22% and improves to 15.0% and 11.0% for optical thickness of 20 and 40. Using cloud transmittance, there is virtually no effective radius information (uncertainty of 71.2%) under a cloud with optical thickness 10. For optically thicker clouds this improved to 51.8% and 14.3% at an optical thickness of 20 and 40, respectively. From Fig. 3 it is evident that the greatest separation between lines of effective radius occurs at optical thickness between 30 and 40. In transmittance, the effective radius uncertainty at an optical thickness of 40 was the minimum. This shows that the sensitivity of transmittance to effective radius is insufficient to retrieve it reliably up to an optical thickness of about 20.

### 3.3 Sensitivity of reflectance and transmittance to effective radius and optical thickness

Figure 4 shows the coalbedo and asymmetry parameter, derived from Mie calculations, across the spectral range of the SSFR/SWS and at three effective radius. The coalbedo increases with increasing effective radius, meaning increased droplet absorption. The asymmetry parameter also increases with increasing effective radius, meaning that forward scattering increases with cloud particle size. The coalbedo varies over several orders of magnitude across this spectral range whereas the asymmetry parameter





ACPD
11, 1053–1104, 2011



changes by only (roughly) 12%. The result is stronger droplet absorption in the near infrared region than in the visible region and a greater spectral dependence in cloud droplet absorption than in scattering.

### 3.4 Transmittance for a range of optical thickness and effective radius

The spectral shapes of the coalbedo and asymmetry parameter have a direct impact on the transmittance. Figure 5 shows modeled transmittance for four values of optical thickness and two values of effective radius. At wavelengths shorter than about 1200 nm the impact of effective radius is predominately due to the direction of scattering (defined by asymmetry parameter). However, because droplet absorption increases with wavelength, the influence of effective radius is eventually dominated by absorption. The transmittance at 515 nm (for example) is greater for a cloud with an effective radius of 25 µm than for 5 µm, a consequence of increased forward scattering by larger particles. At 1628 nm the behavior is reversed: transmittance is greater for a cloud with an effective radius of 5 µm than for 25 µm, a consequence of increased absorption by larger particles. The wavelength at which absorption overtakes scattering can be identified by the crossover between the two spectra calculated with two different effective radius at a single optical thickness. This occurs between 1100 nm and 1400 nm, the exact location being determined by the magnitude of cloud absorption: the greater the absorption (i.e. optically thicker cloud, larger cloud particles, etc.) the shorter the wavelength at which the crossover occurs. By comparison, Fig. 6 shows modeled ice cloud albedo across the spectral range of the SWS/SSFR (from Kindel et al., 2010; the shape of this plot for a liquid water cloud is very similar). The cloud albedo is shown for three effective radius for a given optical thickness. At 500 nm the albedo are grouped by cloud optical thickness and at 2100 nm they are grouped by constant effective radius. In Fig. 5 there is no such grouping with constant effective radius lines, demonstrating that the transmittance depends primarily on optical thickness with only a mild dependence on effective radius throughout this spectral range. This does not mean, however, that optical thickness can be derived from transmittance





ACPD
11, 1053–1104, 2011



without knowledge of the effective radius: Fig. 5 shows that the transmittance value around 500 nm varies considerably, for all values of optical thickness. For an ideal optical thickness retrieval independent of effective radius, those values would need to be identical.

### 3.5 New slope-transmittance retrieval algorithm

It has been shown that the absolute transmittance is relatively insensitive to the effective radius, thus limiting its effectiveness for retrieval of that variable. An alternative to the absolute magnitude of transmittance, made possible by the continuous spectrum provided by SSFR/SWS, is the use of the spectral shape. The strong spectral dependence of the coalbedo makes the liquid water absorbing regions in the near infrared the most favorable choice for improving the effective radius retrieval. One simple parameter to quantify the spectral shape is the slope of transmittance over defined spectral bands. To reduce the error in the linear regression (and thus, in retrieval error) the spectral range over which transmittance was regressed was chosen for linear behavior of transmittance over a wide range of optical thickness and effective radius. As mentioned in Sect. 2.7, the wavelengths must be outside of the bands of strong molecular absorption. Using these criteria and noting the steady decrease in coalbedo with wavelength in the near-infrared, the spectral region between 1565–1634 nm was chosen as the optimum region to apply this method. At the spectral sampling resolution of the SWS, this provided 13 overlapping wavelengths with which to perform the fit.

The slope was calculated by fitting a line to the transmittance normalized by the transmittance at 1565 nm. Due largely to the variability in optical thickness, the absolute transmittance in this spectral sub-range varies by nearly 1 order of magnitude over the optical thickness between 0.1 and 100. Consequently, any slope obtained through a linear regression of absolute transmittance will also vary an order of magnitude. The normalization will largely remove the optical thickness dependence and with it, the dependence of slope on the magnitude of transmittance. In addition to reducing the effects of the optical thickness, normalizing the transmittance reduces the sensitivity to





ACPD
11, 1053–1104, 2011



spectrally neutral calibration errors. The slope from a least-squares linear regression is given by:

$$S_{1565} = \frac{N * \sum_{x=1}^{N} \left[ \lambda_x * \frac{T_x}{T_{1565}} \right] - \sum_{i=0}^{N-1} \lambda_i \sum_{x=0}^{N-1} \frac{T_x}{T_{1565}}}{N * \sum_{x=0}^{N-1} \lambda_x^2 - \left[ \sum_{x=0}^{N-1} \lambda_x \right]^2} \quad (9)$$

where $S_{1565}$ is the slope, $N$ is the number of points used in the fitting, $T$ is the transmittance at each of these points, and $\lambda$ is the wavelength of each point.

The slope retrieval method follows the general procedure outlined in Sect. 2.7. The forward model was used to calculate the transmittance at 515 nm ($T_{515}$) and the spectral slope ($S_{1565}$) as described above. The transmittance and spectral slope from the observations were compared to these forward calculations and a best match was found using a least-squared fit:

$$\chi = \sqrt{\left( \frac{T_{\text{obs},515} - T_{\text{mod},515}}{T_{\text{mod},515}} \right)^2 + \left( \frac{S_{\text{obs},1565} - S_{\text{mod},1565}}{S_{\text{mod},1565}} \right)^2} \quad (10)$$

where $T$ is the transmittance and the subscripts mod and obs refer to modeled and observed, respectively. Figure 7 shows the transmittance at 515 nm plotted against the spectral slope for the same range of optical thickness and effective radius as in Fig. 3. Similar to the dual-wavelength method described previously, the uncertainty in the transmittance and in the normalized transmittance were propagated to $\chi$. The retrieval uncertainties were estimated using the range of optical thickness and effective radius found by minimizing $\chi \pm \delta\chi$. In the slope method, the radiometric uncertainty was assumed to be spectrally neutral. The normalized transmittance is insensitive to this uncertainty and the precision, 0.1% (Pilewskie et al., 2003), was used as the





ACPD
11, 1053–1104, 2011



uncertainty of the normalized transmittance. $\delta\chi$ is determined by

$$\delta\chi = \sqrt{\left(\frac{\partial\chi}{\partial T_{515}}\delta T_{515}\right)^2 + \sum_{x=1}^{N-1}\left(\frac{\partial\chi}{\partial\left(\frac{T_x}{T_{1565}}\right)}\delta\left(\frac{T_x}{T_{1565}}\right)\right)^2} \quad (11)$$

where $\delta\chi$ is the uncertainty in $\chi$ (Eq. 10) and $\delta T$ is the transmittance uncertainty resulting from the 3% radiometric uncertainty, and $\delta(T_x/T_{1565})$ is the 0.1% uncertainty in the normalized transmittance and $N$ is number of wavelengths.

Because of the model assumptions of plain-parallel liquid water clouds, only cloud scenes of this type could be considered. Two filters were imposed on the data to avoid cases that exhibited strong influences from ice particles and scene inhomogeneities. Time periods where these filters failed were not considered.

To avoid erroneous retrievals due to phase differences in the modeled and observed clouds, it was desirable to remove clouds cases that show evidence of ice absorption. Pilewskie and Twomey (1987) and Ehrlich et al. (2008) presented a method of using the spectral slope to retrieve cloud phase information from reflectance observations. A similar but simpler approach was used here to filter out the cases where ice is present. Figure 8 shows the imaginary index of refraction for liquid water and ice, over the spectral region between 1667–1695 nm. The coalbedo $(1-\varpi_0)$, introduced earlier, is linearly proportional to the absorption coefficient $(k)$ and the effective radius in the geometric optics, weak absorption limit, $1-\varpi_0 \propto k r_{\text{eff}}$ (Twomey and Bohren, 1980). The opposite signs of the slopes seen in Fig. 8 for ice and water will result in opposite signs in the slopes of the transmittance. The presence of ice will result in a positive slope in the transmittance in this spectral region. Observations that had a positive slope over this region were not considered.

Clouds are not plane-parallel, as assumed in the forward model, however, clouds scenes can be found that lessen the impact of this assumption by examining the hemispheric irradiance. The hemispheric irradiance encompasses the entire hemisphere ($2\pi$ steradians) above the instrument, as opposed to the much smaller field of view of





ACPD
11, 1053–1104, 2011



the radiance. Using the irradiance measurement can provide more information than the radiance about the entire cloud field. A homogeneous cloud scene will result in a time series that is relatively constant for an extended period of time. A broken cloud field can often be seen as a sudden increase in the time series of the irradiance and can even result in transmitted irradiance that is higher than for clear sky. The time series plots of irradiance were examined by eye for such cases. During ICEALOT irradiance was measured by the SSFR. At the SGP site, the irradiance was measured by the MFRSR. In Fig. 9 the irradiance data from the MFRSR (parts a and b) and the SSFR (part c) are shown for 3 different time periods. Figure 9c shows the irradiance from the SSFR during ICEALOT for a two hour period on 20 March 2008. The data from 16–17 UTC was chosen because it is relatively constant and it avoids the sharp changes that occur before and after. Figure 9a,b shows the MFRSR irradiance from 10 April 2007 and 12 April 2007 over the time period 17.0 to 19.0 UTC. The entire 2 h period from 10 April was chosen. On 12 April, the time period from 17–17.5 UTC and 17.8–18.4 UTC were chosen. There is a slight jump in the irradiance data around 17.75 UTC that corresponds to a period where the clouds broke for a moment. This was verified visually through the images of the total sky imager at the SGP site (not shown). The broken cloud events were excluded from our analysis.

## 4 Retrieval results

The results are presented as comparisons between (1) the retrieval results of the dual-wavelength and the transmittance-slope algorithms, (2) the retrieval uncertainties of the aforementioned algorithms, (3) retrieved optical thickness and effective radius from SWS to retrieved values from MODIS and (4) liquid water path retrieved from the MWR and MODIS and calculated from the SWS retrieved optical thickness and effective radius. There was no MODIS overpass available during the time period chosen from ICEALOT.





ACPD
11, 1053–1104, 2011



### 4.1 ICEALOT retrievals

The ICEALOT data was taken on 20 March 2008 in Long Island Sound. The cloud field in this area would be expected to be heavily polluted and consist of clouds with smaller particles than a cloud with the same LWP in cleaner air. Figure 10a,c shows scatter plots of the retrieved optical thickness and effective radius, respectively. Figure 10b,d shows the histogram and mean of the retrieved optical thickness and effective radius for each of the two methods. The optical thickness histograms for the two retrieval methods were nearly indistinguishable and the scatter plot of the optical thickness from both retrievals line up on the 1:1 line. This is expected given the sensitivity to optical thickness shown in each of the lookup table plots in Fig. 3b and Fig. 7. Figure 10c,d, however, showed a significant difference between the two retrieval methods in the retrieved effective radius. The slope method retrieved smaller average effective radius than the dual-wavelength retrieval with mean effective radius of 12.5 µm and 17 µm, respectively. The majority of the slope retrieved effective radius values lay between 5 µm and 10 µm which would support the expectation of a polluted cloud scene. Each method also retrieved a high number of effective radius at 30 µm. This is the upper end of the library and presumably these values would spread out over larger values if the library were extended.

### 4.2 ARM retrievals

The two days of data from the ARM site were chosen because they exhibited plane-parallel conditions and because they were close enough in time that surface albedo and solar zenith angle would be similar. The comparison plot is shown in Fig. 11 where parts (a) and (c) show scatter plots of the retrieved optical thickness and effective radius values and parts (b) and (d) show histograms of the optical thickness and effective radius values for the two methods, as before. The optical thickness histograms were, again, nearly indistinguishable. The effective radius histograms were slightly more variable than the optical thickness histograms, but the mean retrieved effective radius were





ACPD
11, 1053–1104, 2011



very close, 12.9 µm for the dual-wavelength method and 12.8 µm for the slope method. The clouds in the ARM case are optically thicker than in the ICEALOT case. The mean retrieved optical thickness was 22.5 and 44.4 for the ARM and ICEALOT cases, respectively. The dual-wavelength method is more sensitive to effective radius under these thicker cloud conditions and the agreement between the two retrieval methods is expected.

### 4.3 ICEALOT uncertainty comparisons

The uncertainty estimations outlined previously were used to determine the uncertainty in the retrieved optical thickness and effective radius for each method. In order to determine the relative uncertainties as functions of optical thickness and effective radius, the retrieval uncertainties were averaged for each value of effective radius (1–30 µm) and optical thickness (0.1–0.9, 1–100) in the pre-calculated lookup table. The average effective radius uncertainty and average optical thickness uncertainty were calculated for all retrievals that resulted in an optical thickness of 10, for example, regardless of the occurrences of the accompanying retrieved effective radius. The average uncertainties calculated as a function of optical thickness are not independent of the occurrences of the retrieved effective radius, but nevertheless provide some insight into how the uncertainty varies with optical thickness. These averages are shown in Figs. 12 and 13 for the ICEALOT retrievals and the SGP retrievals, respectively. The average optical thickness uncertainties were never higher than 10% with exceptions of retrievals with the dual-wavelength method when optical thickness is less than 10 and in the case where the effective radius is equal to 16 µm. The latter case results from the lower optical thickness values retrieved for an effective radius of 16 µm with the dual-wavelength method.

The average effective radius uncertainties were more variable, ranging from a few percent up to 30% for the slope method and 50% for the dual-wavelength method. For the ICEALOT retrievals, the slope method resulted in average effective radius uncertainties that were lower than the dual-wavelength method across most of the effective





ACPD
11, 1053–1104, 2011



radius and optical thickness range, the exceptions being optical thickness less than 10 and effective radius larger than 25 µm. Both of these regions are where the effective radius lines in Fig. 7 become less distinguishable.

### 4.4 ARM uncertainty comparisons

The SWS retrieved effective radius uncertainties were lower for the slope method than the dual-wavelength method for optical thickness less than 50. The difference was a factor of 2 at an optical thickness of 20, and decreases with increasing optical thickness. Using the slope method, the average effective radius uncertainties for both the ICEALOT and ARM retrievals were very similar. Under the thicker cloud conditions at the ARM site, the average effective radius uncertainties using the slope method were very similar to the thinner clouds of the ICEALOT case, roughly 10% over most conditions. The dual-wavelength method, however, showed a decrease in effective radius uncertainty from an average of 21% to 12.8% between these two cases, showing again that the optical thickness range for the ARM case does provide increased sensitivity to the cloud particle effective radius.

### 4.5 ICEALOT time series plots

Figure 14 shows time series plots from ICEALOT on 20 March 2008 comparing the retrieved optical thickness, effective radius, derived LWP and estimated retrieval uncertainties for the two different methods. The larger effective radius retrieved by the dual-wavelength method, as compared to the slope method, carried over to the LWP calculations and resulted in higher derived LWP. The mean retrieved LWP was 100 $g/m^2$ for the MWR and 155 $g/m^2$ and 222 $g/m^2$ for the slope and dual-wavelength methods, respectively, using the constant effective radius assumption (Eq. 2). Using the WH06 assumption (Eq. 3), mean retrieved LWP of 129 $g/m^2$ and 185 $g/m^2$ for the slope and dual-wavelength methods were obtained. These results also show that the LWP calculations assuming a WH06 cloud compared better with the MWR retrievals





ACPD
11, 1053–1104, 2011



than the constant effective radius LWP. The LWP derived with the slope method retrievals agreed with the MWR within the uncertainties. Notable exceptions occurred around 16.2 UTC, and during the time period between 16.65 UTC and 16.85. The SSFR retrievals were generally more variable than the MWR retrieved liquid water path. These differences could be the result of vertical and horizontal cloud inhomogeneities. Also, the field of view of these instruments is quite different (3° for the SSFR and 5.7° for the MWR) as are the sampling frequencies (1 s for the SSFR and 16 s for the MWR). These are just two examples of the differences and more work will be needed to pinpoint the differences between these observations, especially with respect to the vertical profile of effective radius and water content.

### 4.6 ARM time series plots

Figure 15 shows a similar time series plot from the SGP site on 10 April 2007. The retrieved optical thickness and effective radius data from the ARM case agreed better than in the ICEALOT case for the two retrieval methods; the agreement between the calculated LWP follows. The MWR and SWS LWP retrievals were within the uncertainty of both methods throughout this time period assuming a WH06 cloud (Eq. 3). The mean retrieved LWP was 272 g/m$^2$ for the MWR and 367 g/m$^2$ and 336 g/m$^2$ for the slope and dual-wavelength methods, respectively, using the constant effective radius assumption. Using the WH06 cloud assumption, the slope method and dual-wavelength mean retrieved LWP values were 306 g/m$^2$ and 280 g/m$^2$.

Figure 16 shows subset of the time series in Fig. 15 from 10 April 2007. The derived LWP from the SWS was calculated using the WH06 assumption. Included with the SWS and MWR retrievals are retrievals from a MODIS overpass. The MODIS 1 km pixel is centered approximately 100 m from the SWS. The MODIS retrieved optical thickness is within 6 of the SWS retrieved optical thickness and within the MODIS and SWS uncertainties. The MODIS retrieved effective radius is also within the uncertainty of both the dual-wavelength and slope retrievals.





ACPD
11, 1053–1104, 2011



Figure 17 shows another subset of data from 10 April 2007 (Fig. 15) that includes a second MODIS overpass. In this case the MODIS optical thickness and SWS optical thickness differed by about 20, exceeding the uncertainty of the respective retrievals. The MODIS effective radius was within the uncertainty of the slope method, but outside the uncertainty of the dual-wavelength method. The dual-wavelength LWP was within the uncertainty of the MODIS retrieval despite the fact that the optical thickness and the effective radius were not. For this MODIS overpass, the SWS was located in the corner of the 1 km MODIS pixel. Table 2 shows the retrieved optical thickness for the MODIS pixels for the two cases presented in Figs. 16 and 17. In the case centered at 18.86 UTC (Fig. 16) the surrounding MODIS pixels have retrieved values for optical thickness that were within 4 of the pixel over the SWS. The second case, centered at 17.21 UTC (Fig. 17), the SWS was towards one corner of the pixel and the closest adjacent MODIS pixel has a retrieved optical thickness of 38.04. This suggests that the reason for the MODIS-SWS disagreement is a less homogeneous cloud field coupled with the different fields of view of the instruments.

## 5 Conclusions

A new multispectral algorithm using cloud transmittance was presented to retrieve cloud optical thickness and cloud particle effective radius. The algorithm uses the continuous spectrum measured by the SSFR/SWS instruments and exploits the spectral shape to increase the sensitivity to the effective radius. The spectral shape was quantified by fitting the slope to the normalized transmittance between 1565 nm and 1634 nm. The algorithm used this slope in combination with the transmittance at 515 nm. The retrieval was performed by fitting the observed slope and transmittance to a library of pre-calculated values. In addition, the liquid water path was derived from the retrieved optical depth and effective radius for two different vertical distributions of effective radius, (1) effective radius constant with cloud height, and (2) for a WH06 cloud. The radiometric uncertainty was propagated through the fitting algorithm and the resulting





ACPD
11, 1053–1104, 2011



range of optical thickness and effective radius was used to estimate the retrieval uncertainty.

A series of model calculations were used to elucidate the relationships between cloud transmittance and optical thickness and effective radius. It was shown that cloud transmittance is less sensitive to the effective radius than cloud reflectance and, unlike cloud reflectance, transmittance is mostly sensitive to the optical thickness over the spectral range of the SSFR/SWS. A dual-wavelength retrieval was modeled using the radiative transfer model calculations and corresponding uncertainties were calculated to quantify the uncertainty in retrieved effective radius. It was found that the dual-wavelength method provides virtually no effective radius information for optical thickness near 10, but for optically thicker cases, between 20 and 40, the sensitivity to effective radius nearly matches that of cloud reflectance.

The slope retrieval and the dual-wavelength retrieval were both applied to data from the ARM SGP facility and ICEALOT. The retrieved results and estimated uncertainties from these methods were compared. The results showed that for the ARM case the average retrieved effective radius and optical thickness from the two methods were virtually identical with slightly higher (12.8% vs. 8.9%) effective radius uncertainties with the dual-wavelength method. For the thinner cloud scene in the ICEALOT case the dual-wavelength method retrieved higher effective radius values and higher effective radius uncertainties. The optical thickness retrievals were again virtually identical. The average derived LWP using the WH06 cloud was within 12.5% and 20% of the MWR LWP for the ARM and ICEALOT data. This agreed better than the average constant effective radius LWP which was within 35% and 55% of the average MWR LWP for the ARM and ICEALOT data. For the ARM case, the derived LWP using the WH06 cloud was within the uncertainty of the two retrieval methods over the two hour period but for the ICEALOT case, it was within the uncertainties for much of the one hour period, but did result in some differences. Explaining these differences will take more investigation. Retrievals from two MODIS overpasses over the ARM site were also compared to the SWS retrievals. The MODIS pixels surrounding the site showed a more homogeneous





ACPD
11, 1053–1104, 2011



cloud scene in the case centered at 18.86 UTC and in this case the SWS retrieved results were within the uncertainty of the MODIS results. The second case, centered at 17.21 UTC, was less homogeneous than the first case and the agreement between the SWS and MODIS retrievals did not agree as well.

Future work with slope retrieval algorithm will continue to improve and better characterize its ability to retrieve optical thickness and effective radius. Possible improvements include replacing the use of the transmittance at 515 nm in the algorithm with another slope and adding data in the spectral region near 2.1 µm. Replacing the transmittance at 515 nm with another slope could make the algorithm even less sensitive independent of the spectrally-neutral radiometric uncertainty. The spectral region near 2.1 µm could provide more sensitivity to the effective radius. To improve the characterization of the algorithm the uncertainty calculations can be improved by using a more thorough analysis as in Vukicevic et al. (2010). The retrieval sensitivity to the model assumptions, such as the surface albedo and cloud geometry, will be quantified. In addition to exploring improvements to the algorithm, continued application of the algorithm with different experiments is planned and comparisons with other retrievals methods will continue.

## References


Barker, H. W. and Marshak, A.: Inferring optical depth of broken clouds above green vegetation using surface solar radiometric measurements, J. Atmos. Sci., 58, 2989–3006, 2001.

Bergstrom, R. W., Pilewskie, P., Schmid, B., and Russell, P. B.: Estimates of the spectral aerosol single scattering albedo and aerosol radiative effects during SAFARI 2000, J. Geophys. Res., 108, 8474, 2003.

Chiu, J. C., Huang, C., Marshak, A., Slutsker, I., Giles, D. M., Holben, B. N., Knyazikhin, Y., and Wiscombe, W. J.: Cloud optical depth retrievals from the Aerosol Robotic Network (AERONET) cloud mode observations, J. Geophys. Res., 115, D14202, 2010.

Clark, R. N., Swayze, G. A., Wise, R., Livo, E., Hoefen, T., Kokaly, R., and Sutley, S. J.: USGS digital spectral library splib06a: US Geological Survey, Digital Data Series 231, 2007.

Coddington, O., Schmidt, K. S., Pilewskie, P., Gore, W. J., Bergstrom, R. W., Román, M., Rede-






ACPD
11, 1053–1104, 2011



mann, J., Russell, P. B., Liu, J., and Schaaf, C. C.: Aircraft measurements of spectral surface albedo and its consistency with ground-based and space-borne observations, J. Geophys. Res.-Atmos., 113, D17209, 2008.

Ehrlich, A., Bierwirth, E., Wendisch, M., Gayet, J.-F., Mioche, G., Lampert, A., and Heintzenberg, J.: Cloud phase identification of Arctic boundary-layer clouds from airborne spectral reflection measurements: test of three approaches, Atmos. Chem. Phys., 8, 7493–7505, doi:10.5194/acp-8-7493-2008, 2008.

Forster, P., Ramaswamy, V., Artaxo, P., Berntsen, T., Betts, R., Fahey, D. W., Haywood, J., Lean, J., Lowe, D. C., Myhre, G., Nganga, J., Prinn, R., Raga, G., Schulz, M., and Van Dorland, R.: Changes in Atmospheric Constituents and in Radiative Forcing, in: Climate Change 2007: The Physical Science Basis. Contribution of Working Group I to the Fourth Assessment Report of the Intergovernmental Panel on Climate Change, edited by: Solomon, S., Qin, D., Manning, M., Chen, Z., Marquis, M., Averyt, K. B., Tignor, M., and Miller, H. L., Cambridge University Press, Cambridge, UK and New York, NY, USA, 131–217, 2007.

Hansen, J. E. and Hovenier, J. W.: Interpretation of the polarization of Venus, J. Atmos. Sci., 31, 1137–1160, 1974.

Hansen, J. E. and Pollack, J. B.: Near-infrared light scattering by terrestrial clouds, J. Atmos. Sci., 27, 265–281, 1970.

Harrison, L., Michalsky, J., and Berndt, J.: Automated multifilter rotating shadow-band radiometer: an instrument for optical depth and radiation measurements, Appl. Opt., 33, 5118–5125, 1994.

Holben, B.: AERONET: A federated instrument network and data archive for aerosol characterization, Remote Sens. Environ., 66, 1–16, 1998.

Kikuchi, N., Nakajima, T., Kumagai, H., Kuroiwa, H., Kamei, A., Nakamura, R., and Nakajima, T. Y.: Cloud optical thickness and effective particle radius derived from transmitted solar radiation measurements: comparison with cloud radar observations, J. Geophys. Res., 111, D07205, 2006.

Kindel, B. C., Schmidt, K. S., Pilewskie, P., Baum, B. A., Yang, P., and Platnick, S.: Observations and modeling of ice cloud shortwave spectral albedo during the Tropical Composition, Cloud and Climate Coupling Experiment (TC4), J. Geophys. Res., 115, D00J18, 2010.

King, M. D., Menzel, P. W., Grant, P. S., Myers, J. S., Arnold, T. G., Platnick, S. E., Gumley, L. E., Tsay, S., Moeller, C. C., Fitzgerald, M., Brown, K. S., and Osterwisch, F. G.: Airborne Scanning Spectrometer for remote sensing of cloud, aerosol, water vapor, and surface properties,





ACPD
11, 1053–1104, 2011



J. Atmos. Ocean. Tech., 13, 777–794, 1996.
Leontyeva, E. and Stamnes, K.: Estimations of cloud optical thickness from ground-based measurements of incoming solar radiation in the Arctic, J. Climate, 7, 566–578, 1994.
Liljegren, J. C. and Lesht, B. M.: Measurements of integrated water vapor and cloud liquid water from microwave radiometers at the DOE ARM Cloud and Radiation Testbed in the US Southern Great Plains, in: IEEE International Geosciences and Remote Sensing Symposium (IGARSS), Lincoln, NE, 21–26 May 1996, 1675–1677, 1996.
Marshak, A., Knyazikhin, Y., Evans, K. D., and Wiscombe, W. J.: The RED versus NIR plane to retrieve broken-cloud optical depth from ground-based measurements, J. Atmos. Sci., 61, 1911–1925, 2004.
Nakajima, T. and King, M. D.: Determination of the optical thickness and effective particle radius of clouds from reflected solar radiation measurements. Part I: Theory, J. Atmos. Sci., 47, 1878–1893, 1990.
Pilewskie, P. and Twomey, S.: Cloud phase discrimination by reflectance measurements near 1.6 and 2.2 µm, J. Atmos. Sci., 44, 1987.
Pilewskie, P., Pommier, J., Bergstrom, R., Gore, W., Howard, S., Rabbette, M., Schmid, B., Hobbs, P. V., and Tsay, S. C.: Solar spectral radiative forcing during the Southern African Regional Science Initiative, J. Geophys. Res., 108, 8486, 2003.
Platnick, S.: Vertical photon transport in cloud remote sensing problems, J. Geophys. Res., 105, 22919–22935, 2000.
Platnick, S., King, M. D., Ackerman, S. A., Menzel, W. P., Baum, B. A., Riédi, J. C., and Frey, R. A.: The MODIS Cloud Products: Algorithms and Examples From Terra, IEEE T. Geosci. Remote, 41, 459–473, 2003.
Rawlins, F. and Foot, J. S.: Remotely sensed measurements of stratocumulus properties during FIRE using the C130 aircraft multi-channel radiometer, J. Atmos. Sci., 47, 2488–2504, 1990.
Schiffer, R. A. and Rossow, W. B.: The International Satellite Cloud Climatology Project (ISCCP): The first project of the world climate research programme, B. Am. Meteorol. Soc., 64, 779–784, 1983.
Stokes, G. M. and Schwartz, S. E.: The Atmospheric Radiation Measurement (ARM) program: programmatic background and design of the cloud and radiation test bed, B. Am. Meteorol. Soc., 75, 201–1222, 1994.
Taylor, J. R.: An Introduction to Error Analysis: The Study of Uncertainties in Physical Measurements, 2nd edn., University Science Books, Sausalito, California, 1996.





ACPD
11, 1053–1104, 2011



Twomey, S. and Bohren, C. F.: Simple approximations for calculations of absorption in clouds, J. Atmos. Sci., 37, 2086–2095, 1980.

Twomey, S. and Cocks, T.: Remote sensing of cloud parameters from spectral reflectance in the near-infrared, Beitr. Phys. Atmos., 62, 172–179, 1989.

Vukicevic, T., Coddington, O., and Pilewskie, P.: Characterizing the retrieval of cloud properties from optical remote sensing, J. Geophys. Res., 115, D20211, 2010.

Westwater, E. R.: Ground-Based Microwave Remote Sensing of Meteorological Variables, Atmospheric Remote Sensing By Microwave Radiometry, edited by: Janssen, M. A., Wiley, New York, NY, 145–207, 1993.

Westwater, E. R., Han, Y., Shupe, M. D., and Matrosov, S. Y.: Analysis of integrated cloud liquid and precipitable water vapor retrievals from microwave radiometers during the Surface Heat Budget of the Arctic Ocean project, J. Geophys. Res., 106, 32019–32030, 2001.

Wood, R. and Hartmann, D. L.: Spatial variability of liquid water path in marine low cloud: the importance of mesoscale cellular convection, J. Climate, 19, 1748–1764, 2006.





ACPD

11, 1053–1104, 2011



**Table 1.** Relative optical thickness ($\tau$) and effective radius ($r_{eff}$) uncertainties calculated from simulated retrievals for cloud reflectance and transmittance. The uncertainties were calculated by propagating the 3% radiometric uncertainty through the retrieval algorithm.

| | | Reflectance retrievals | | Transmittance retrievals | |
|---|---|---|---|---|---|
| $\tau$ | $r_{eff}$ (μm) | Relative $\tau$ uncertainty (%) | Relative $r_{eff}$ uncertainty (%) | Relative $\tau$ uncertainty (%) | Relative $r_{eff}$ uncertainty (%) |
| 10 | 10 | 5.7 | 22 | 14.9 | 71.2 |
| 20 | 10 | 8.0 | 15.0 | 6.8 | 51.8 |
| 40 | 10 | 12.2 | 11.0 | 2.3 | 14.3 |





ACPD
11, 1053–1104, 2011



**Table 2.** MODIS optical thickness retrievals taken on 10 April 2007. The center cell of the each table show the MODIS retrieved optical thickness for the MODIS pixel that is above the SWS. The rest of the cells show the surrounding MODIS pixels.

| (a) MODIS optical thickness retrievals for 18.86 UTC | | | (b) MODIS optical thickness retrievals for 17.21 UTC | | |
|---|---|---|---|---|---|
| 46.56 | 46.43 | 46.45 | 34.6 | 35.09 | 33.32 |
| 45.42 | 45.63 | 44.88 | 38.86 | 31.28 | 31.64 |
| 48.93 | 45.84 | 44.45 | 38.04 | 37.39 | 36.74 |





ACPD
11, 1053–1104, 2011



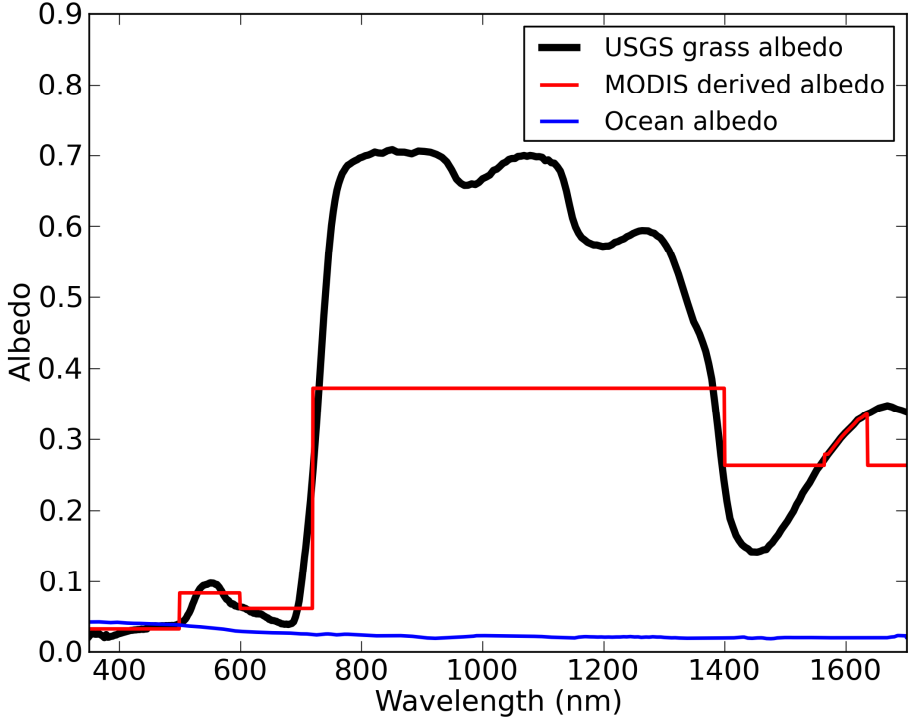


**Fig. 1.** Surface albedo for a green surface, the parameterized MODIS surface albedo, and the ICARTT ocean albedo used in the radiative transfer model.





ACPD
11, 1053–1104, 2011



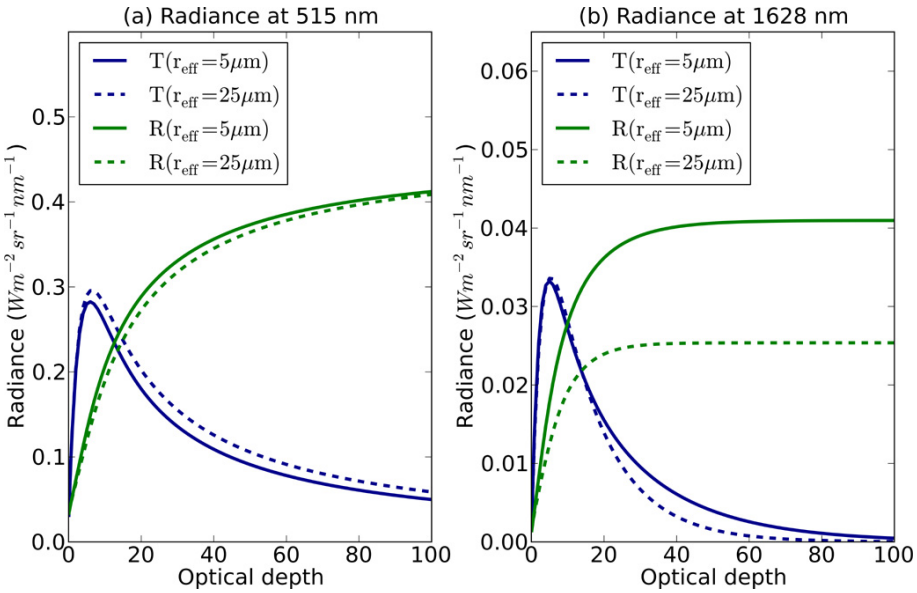


**Fig. 2.** Modeled transmitted (blue) and reflected (green) radiance at **(a)** 515 nm and **(b)** 1628 nm for effective radius values of 5 µm (solid lines) and 25 µm (dashed lines).





ACPD
11, 1053–1104, 2011



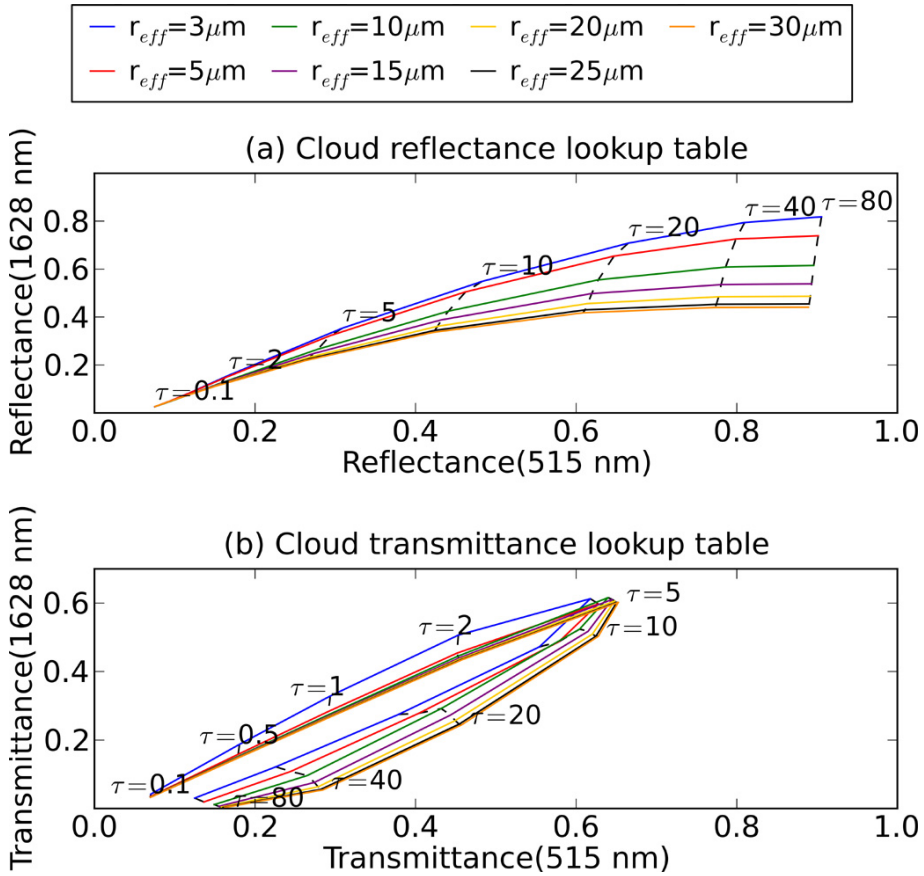


**Fig. 3.** Lookup table for a dual channel retrieval method using **(a)** cloud reflectance and **(b)** cloud transmittance. Constant effective radius lines are solid and constant optical thickness lines are dashed.





ACPD
11, 1053–1104, 2011





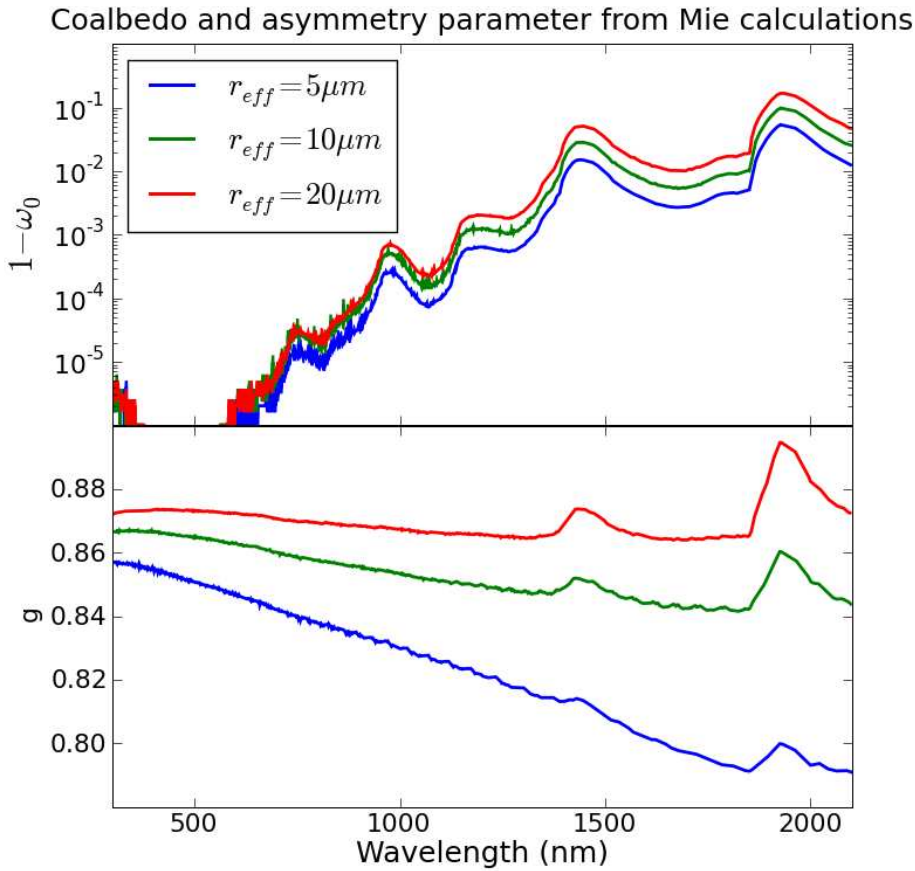


**Fig. 4.** Coalbedo and asymmetry parameter for liquid water drops from Mie calculations for three different cloud particle effective radius.





ACPD
11, 1053–1104, 2011



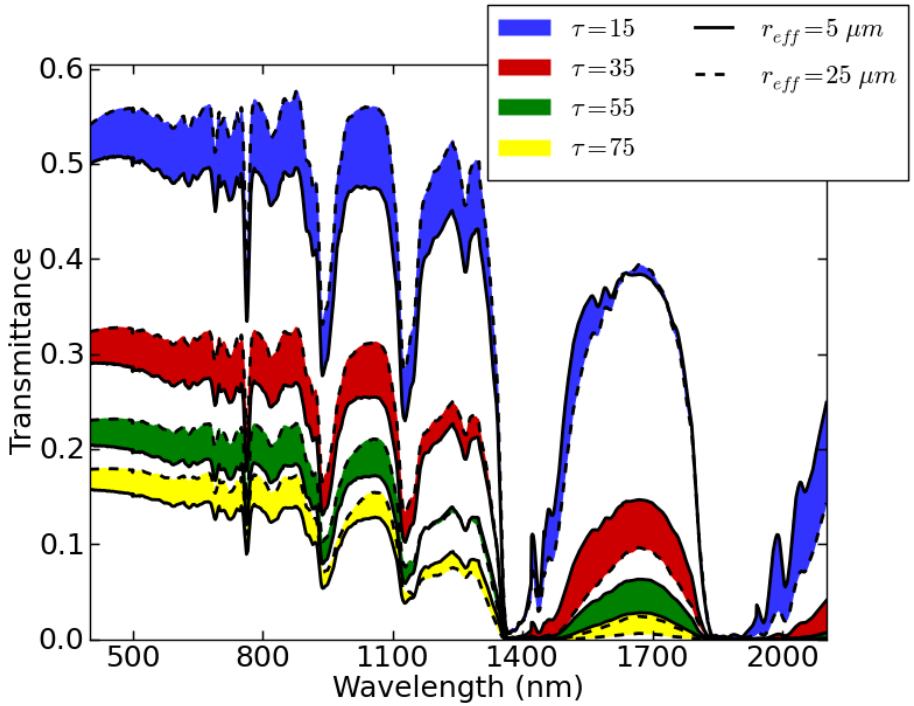


**Fig. 5.** Modeled transmittance through a liquid water cloud showing the dependencies on cloud optical thickness and cloud particle effective radius. The shaded regions are that of constant cloud optical thickness for a cloud particle effective radius range spanning from 5–25 µm.





ACPD
11, 1053–1104, 2011



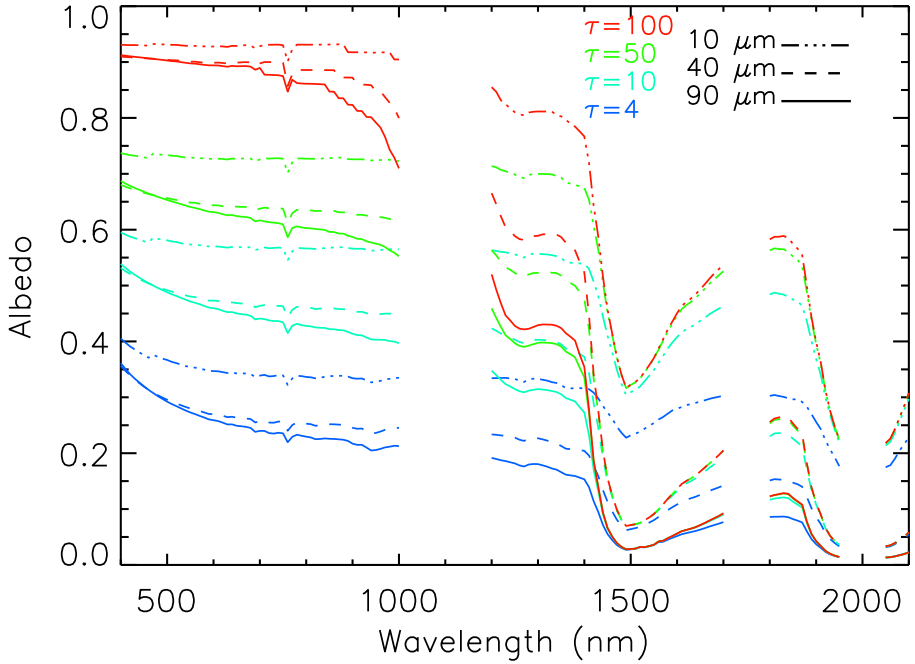


**Fig. 6.** Modeled albedo of an ice cloud showing the dependencies on cloud optical thickness and cloud particle effective radius. Each color represents the spectral albedo of constant optical depth and each line style represents the spectral albedo of constant effective radius (Kindel et al., 2010).





ACPD
11, 1053–1104, 2011



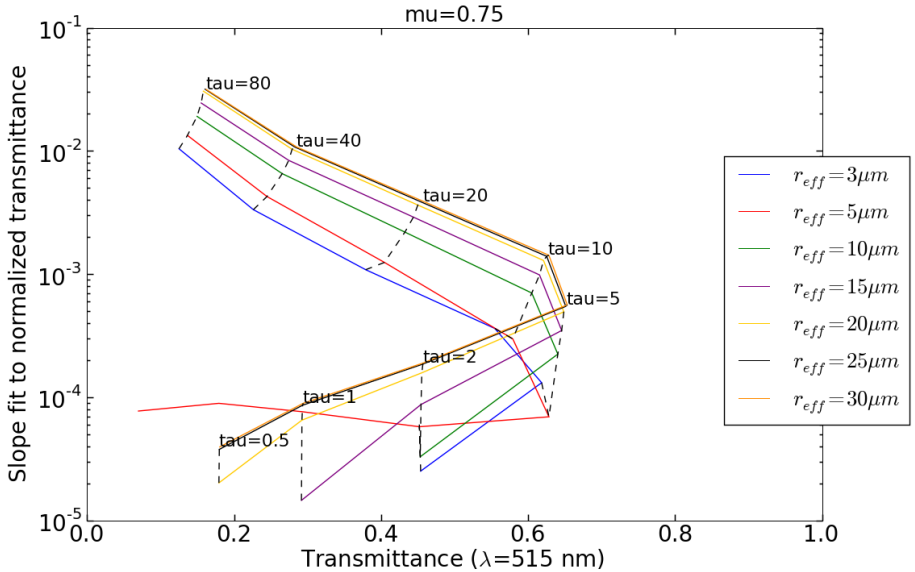


**Fig. 7.** Look up table using the transmittance calculated with modeled surface radiance and the slope of the line fit through the normalized transmittance in the range 1565–1634 nm.





ACPD
11, 1053–1104, 2011





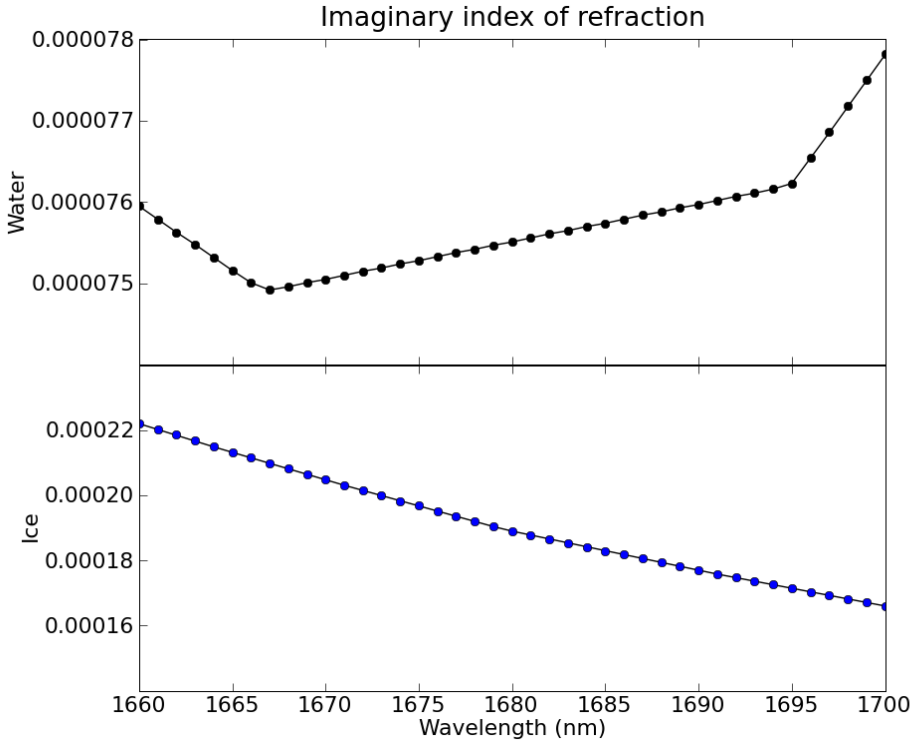


**Fig. 8.** The imaginary index of refraction of liquid water and ice over a short range in the near infrared.





ACPD
11, 1053–1104, 2011



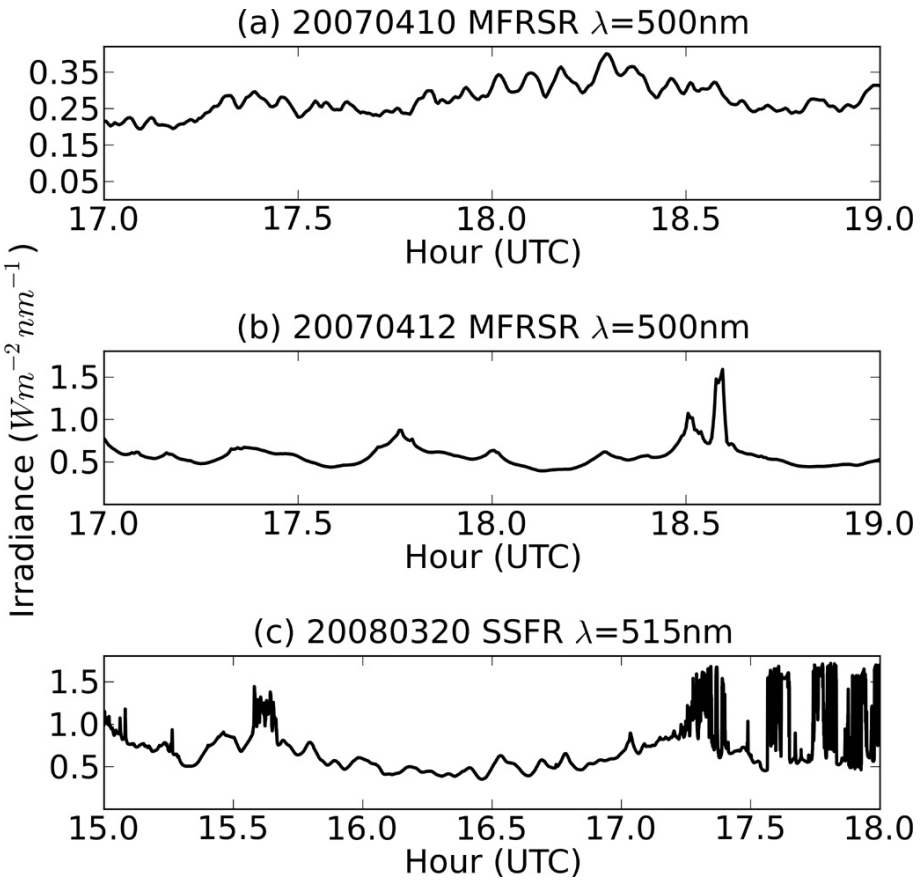


**Fig. 9.** Time series observations of irradiance from the MFRSR (**a** and **b**) and the SSFR **(c)**.





ACPD
11, 1053–1104, 2011



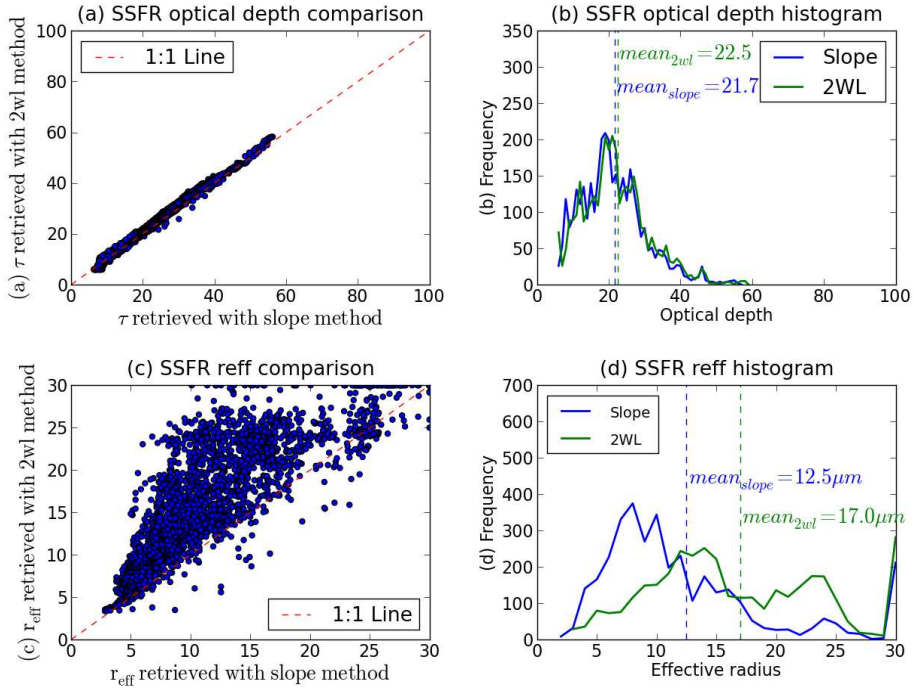


**Fig. 10.** Cloud parameter retrieval results comparing the slope method to the dual-wavelength retrieval method. Shown are **(a)** scatter plot of the retrieved optical thickness for the two methods, **(b)** a histogram of the retrieved optical thickness for both methods, **(c)** scatter plot of the retrieved effective radius for the two methods, and **(d)** a histogram of the retrieved effective radius for both methods.





ACPD
11, 1053–1104, 2011



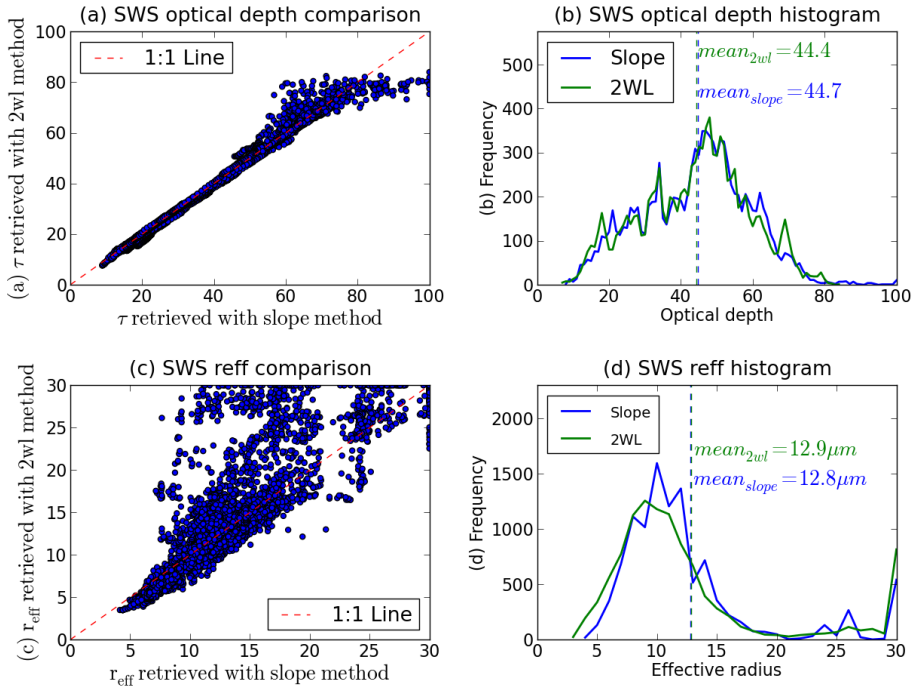


**Fig. 11.** Cloud parameter retrieval results comparing the slope method to the dual-wavelength retrieval method. Shown are **(a)** scatter plot of the retrieved optical thickness for the two methods, **(b)** a histogram of the retrieved optical thickness for both methods, **(c)** scatter plot of the retrieved effective radius for the two methods, and **(d)** a histogram of the retrieved effective radius for both methods.





ACPD
11, 1053–1104, 2011



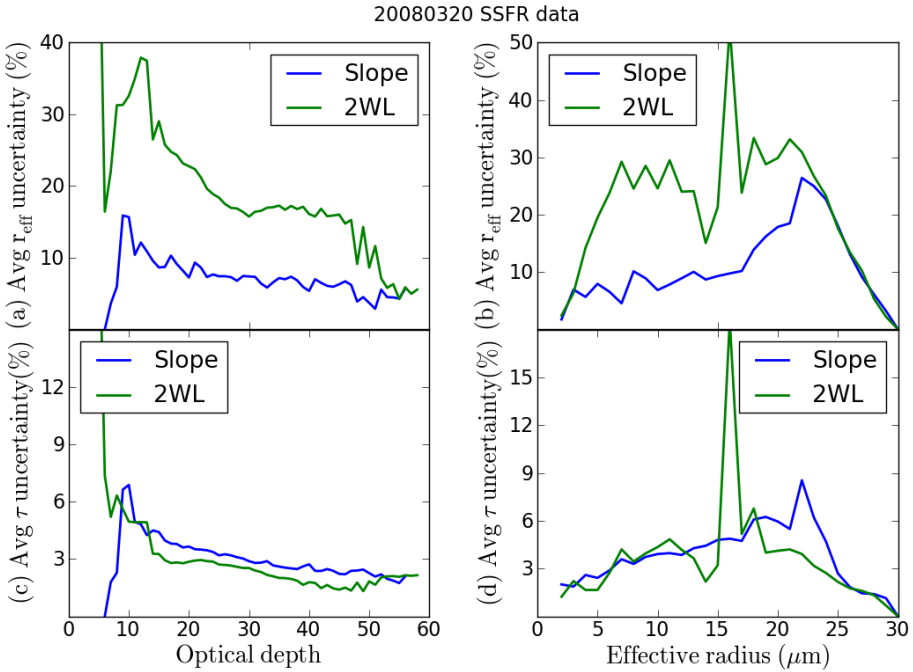


**Fig. 12.** Uncertainty calculations for effective radius (top row) and optical thickness (bottom row) versus optical thickness (left column) and effective radius (right column).





ACPD
11, 1053–1104, 2011



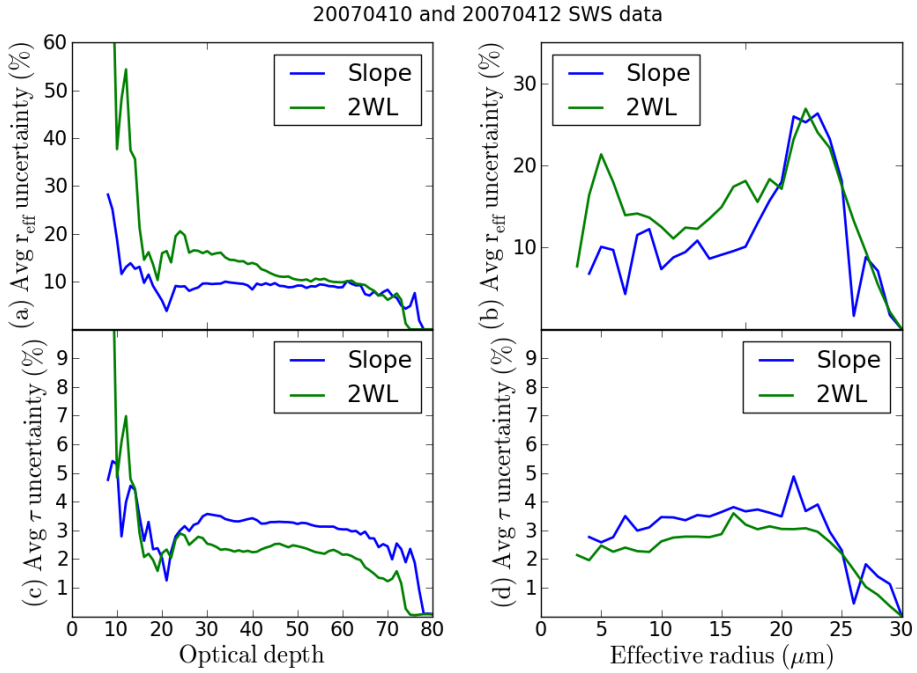


**Fig. 13.** Uncertainty calculations for effective radius (top row) and optical thickness (bottom row) versus optical thickness (left column) and effective radius (right column).





ACPD
11, 1053–1104, 2011



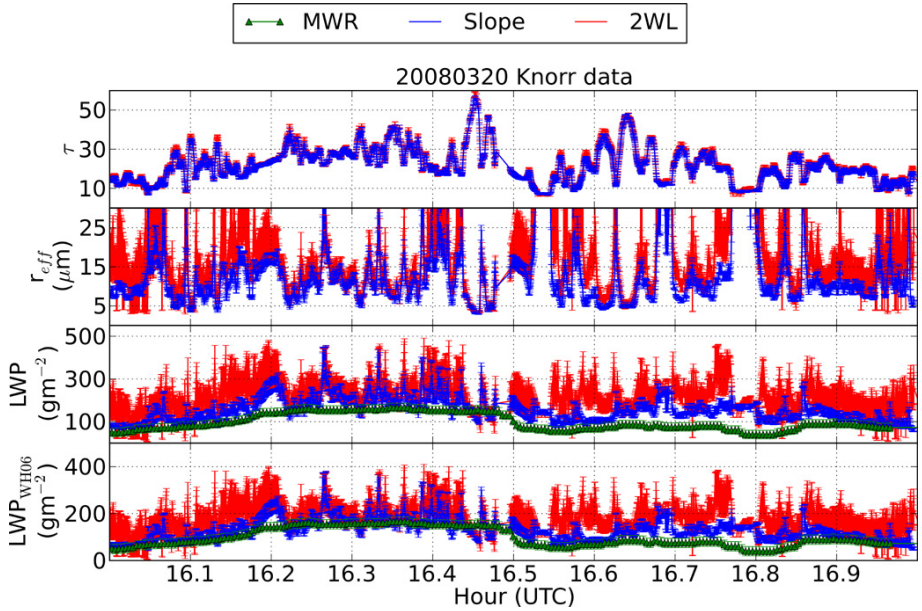


**Fig. 14.** Time series plots of SSFR retrievals of optical thickness and effective radius. LWP retrievals from the NOAA MWR along with calculated LWP from SSFR retrievals. Each point is shown with its estimated uncertainty.





ACPD
11, 1053–1104, 2011



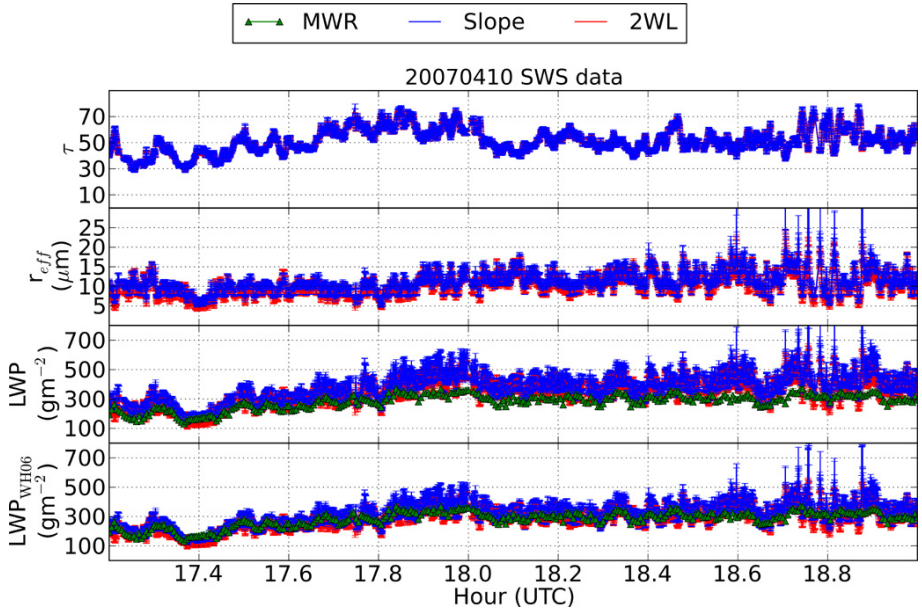


**Fig. 15.** Time series plots of SWS retrievals of optical thickness and effective radius. LWP retrievals from the ARM MWR along with calculated LWP from SWS retrievals. Each point is shown with its estimated uncertainty.





ACPD
11, 1053–1104, 2011



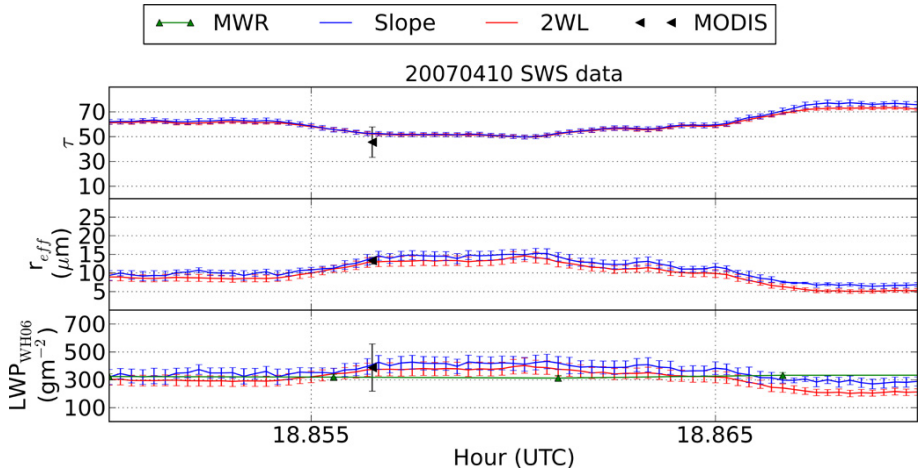


**Fig. 16.** Time series plots of SWS retrievals of optical thickness and effective radius from SWS and MODIS. LWP retrievals from the ARM MWR and MODIS along with calculated LWP from SWS retrievals.





ACPD
11, 1053–1104, 2011



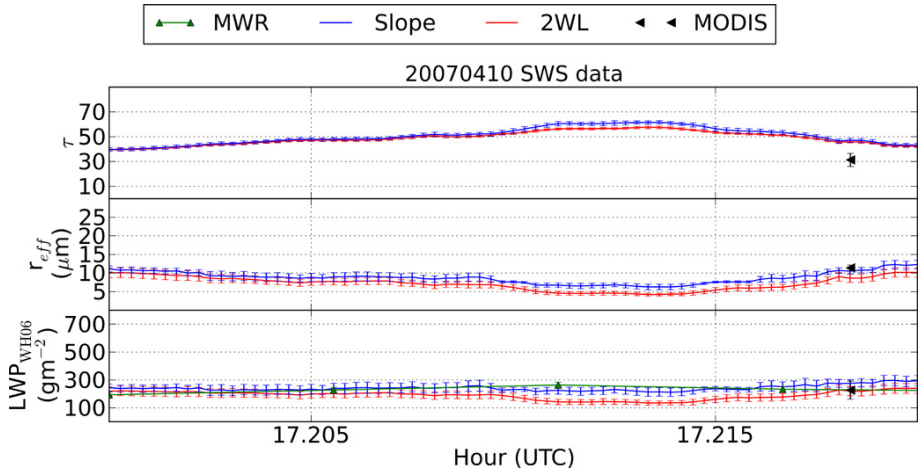


**Fig. 17.** Time series plots of SWS retrievals of optical thickness and effective radius from SWS and MODIS. LWP retrievals from the ARM MWR and MODIS along with calculated LWP from SWS retrievals.





ACPD
11, 1053–1104, 2011